APPLIED PHYSICS

Acoustohydrodynamic tweezers via spatial arrangement of streaming vortices

Haodong Zhu[1], Peiran Zhang[1], Zhanwei Zhong[2], Jianping Xia[1], Joseph Rich[3], John Mai[4], Xingyu Su[1], Zhenhua Tian[1], Hunter Bachman[1], Joseph Rufo[1], Yuyang Gu[1], Putong Kang[1], Krishnendu Chakrabarty[2], Thomas P. Witelski[5], Tony Jun Huang[1]*

Acoustics-based tweezers provide a unique toolset for contactless, label-free, and precise manipulation of bioparticles and bioanalytes. Most acoustic tweezers rely on acoustic radiation forces; however, the accompanying acoustic streaming often generates unpredictable effects due to its nonlinear nature and high sensitivity to the three-dimensional boundary conditions. Here, we demonstrate acoustohydrodynamic tweezers, which generate stable, symmetric pairs of vortices to create hydrodynamic traps for object manipulation. These stable vortices enable predictable control of a flow field, which translates into controlled motion of droplets or particles on the operating surface. We built a programmable droplet-handling platform to demonstrate the basic functions of planar-omnidirectional droplet transport, merging droplets, and in situ mixing via a sequential cascade of biochemical reactions. Our acoustohydrodynamic tweezers enables improved control of acoustic streaming and demonstrates a previously unidentified method for contact-free manipulation of bioanalytes and digitalized liquid handling based on a compact and scalable functional unit.

INTRODUCTION

Acoustics-based tweezers recently attracted the attention of the biomedical research community as a versatile toolset for the manipulation of bioparticles with unprecedented flexibility and biocompatibility. Among the various particle manipulation techniques, including optical (1), electrical (2–6), and hydrodynamic force–based methods (7, 8), acoustics-based tweezers exhibit the unique combination of advantages including versatile particle manipulation, contactless modality that minimizes cross contamination, and biocompatibility (9–11) in terms of handling fragile samples such as exosomes, stem cells, zebrafish, and embryos. Now, most well-established acoustics-based tweezers rely on acoustic radiation forces as the main driving forces for particle manipulation (12–23). However, precise control of the accompanying effect of, and interactions due to, acoustic streaming has not been explored in detail. Acoustic streaming is the steady flow generated by wave propagation in a fluid after attenuation by viscous forces. Because of complex flow interactions, acoustic streaming will usually lead to chaotic mixing, which is generally considered as a "noise" effect and will counteract the acoustic radiation forces. However, because of the inherent nonlinear properties and high sensitivity to changes in three-dimensional (3D) boundary conditions, the precise, predictable, and robust control of acoustic streaming has yet to be realized. The lack of robust control of acoustic streaming limits the use of acoustic streaming in many practical applications.

Recently, there have been several studies to develop acoustic streaming tweezers to achieve controllable particle manipulation (24–26). For example, several strategies passively use the streaming vortices accompanying acoustic wave propagation for size-selective microparticle separation (27, 28). Following a different device con-

figuration, arrays of fixed hydrodynamic stagnation points can be generated using oscillating structures with tuned boundaries for on-demand particle trapping (29, 30). In contrast to those passive methods, active control strategies move objects with dynamic programmability by switching localized streaming patterns in a stepwise manner (31, 32). However, because of the inherent nonlinear properties of acoustic streaming, precise control of the fluid field in acoustic streaming tweezers has so far eluded researchers, thus limiting robust object manipulation and attempts at control optimization. Specifically, most existing acoustic streaming tweezer designs rely on the spontaneous phenomena of acoustic streaming that accompanies wave propagation and lacks guidelines or verified theories for decomposing and controlling acoustic streaming with dynamic reconfigurability.

Here, we demonstrate a contactless, label-free, and precise acoustohydrodynamic tweezer (AHT) platform for noninvasive handling of droplets and solid particles based on shaped acoustic streaming. An array of upright, thin piezoelectric (PZT) plates arranged in an alternating and mutually orthogonal pattern generate stable acoustic streaming vortices in a liquid, dynamic control, and accurate prediction of the resulting flow fields on an oil surface via the combination of the induced speed from these vortices. These thin PZT plates, arranged in a periodic spatial pattern, are submerged in an oil layer. The PZT plates act as both acoustic wave generators and boundaries to confine and shape the 3D acoustic streaming. This PZT array enables the stable generation of hydrodynamic wells that act as trapping points on the oil surface (also generically referred to as the "working surface"). The PZT array also enables the accurate prediction of the movement of these hydrodynamic traps during multiunit actuation. Compared with existing fluidic processing methods, precise manipulation of the flow field is achieved by actuating single or multiple upright PZT plates at the same time. This unique design for the AHT platform greatly increases the efficiency and robustness of the complex manipulation of floating objects. Furthermore, the scalable array pattern and digital electronic control system allow a high level of flexibility, which accommodates

[1]Department of Mechanical Engineering and Material Science, Duke University, Durham, NC 27708, USA. [2]Department of Electrical and Computer Engineering, Duke University, Durham, NC 27708, USA. [3]Department of Biomedical Engineering, Duke University, Durham, NC 27708, USA. [4]Alfred E. Mann Institute for Biomedical Engineering, University of Southern California, Los Angeles, CA 90089, USA. [5]Department of Mathematics, Duke University, Durham, NC 27708, USA.
*Corresponding author. Email: tony.huang@duke.edu

a wide range of droplet volumes (from several nanoliters to hundreds of microliters). This platform also allows for the parallel manipulation of droplets along reusable fluidic routes via digital programming. This rewritability contributes to a compact platform. We have developed a simple and effective small-scale (4 × 4 units) prototype AHT platform with a high actuation speed (i.e., <5 s for each step) at a lower voltage input (8 Vpp per unit, where Vpp stands for peak-to-peak voltage) than current acoustic tweezers, with simple fabrication and a low variance between experiments (<2% coefficient of variation). With an optimized vertical configuration of PZT plates, this platform has potential applications for large-scale drug screening and biosample testing due to its ability to perform multistep cascades of reactions.

RESULTS

Establishing a single acoustohydrodynamic well for trapping droplets

The prototype AHT platform (Fig. 1A) contains an array of 4 × 4 PZT units submerged in a carrier fluid of a dense oil layer. Each upright PZT plate is surrounded by eight solid barriers (which are either the surrounding PZTs or static plastic plates), maintaining an alternating and mutually orthogonal barrier pattern. With this specific arrangement, when an upright PZT is actuated and vibrates in the bending mode, a pair of stable acoustic streaming vortices will be generated on both sides of its center. These stable acoustic streaming vortices consistently creates a hydrodynamic well with a specific flow pattern above the upright PZT (i.e., a trapping "unit" in the platform; Fig. 1B). As the actuated upright PZTs can attract objects located above nearby units, this omnidirectional attraction acts as a manipulation method for objects floating on the carrier fluid. Accordingly, when this hydrodynamic trap is programmed to actuate in a sequential manner by selectively controlling the on/off status (or 0/1 states) of different PZT units, it can move various types of objects floating on the carrier fluid, including water or oil droplets, polystyrene particles, or zebrafish in phosphate-buffered saline (PBS) buffer in a specific path (Fig. 1, C to H, and movie S1). With this scaled-up AHT platform fabricated and each upright PZT unit uniformly connected to a radio frequency power source, each PZT unit is actuated in a programmed sequence manner to move the object floating on the oil surface (note S1 and fig. S1).

The stable vortex pair generated by the AHT unit is an important consequence of this modified acoustic streaming. Experimentally, we found that if a PZT plate is submerged into any type of carrier fluid (such as water or oil) and set upright with respect to the bottom plate, a clover-shaped flow pattern will be generated when the transducer is actuated (fig. S2). In this initial flow mode, fluid is pumped out by the actuating upright PZT in the direction vertical to the plate surface (labeled as the y direction) because of the continuous and oscillatory pressure fields generated in the plane parallel to the upright PZT surface. The fluid then flows back in the direction parallel to the plate surface (labeled as the x direction). Hydrodynamic forces generated by this stable flow pattern create a stagnation point above the center of the upright PZT unit in the liquid-air interface of the base fluid, in the x direction. However, this stagnation point is an unstable hydrodynamic saddle point in the flow field with flow being attracted in the $\pm x$ directions and flow being repelled in the $\pm y$ directions.

To examine how this flow pattern is modified inside a single unit, we leveraged the symmetry of the system and only needed to model
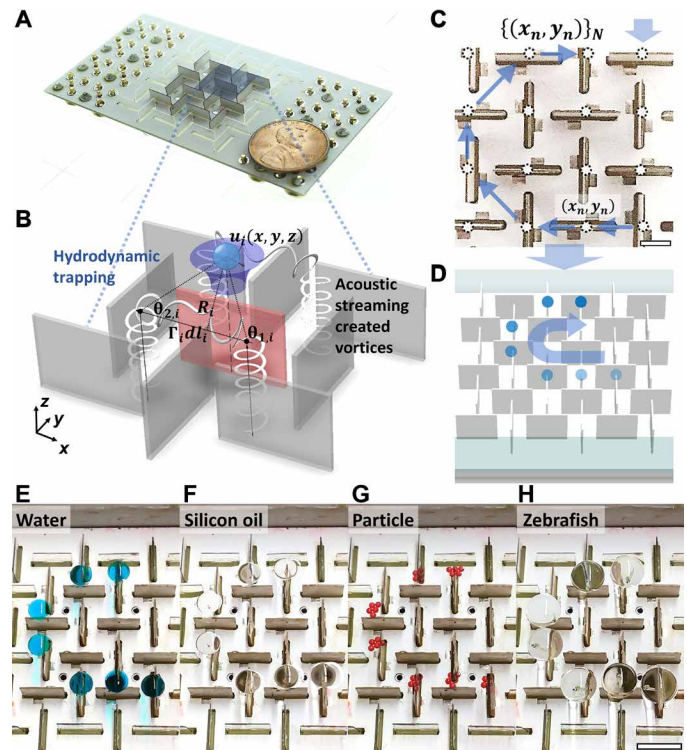

Fig. 1. Schematics of an AHT prototype composed of 4 × 4 upright PZT units. (**A**) Image of the prototype with four active PZT plates surrounded by static plastic barriers, where each PZT plate is the center of a unit of the AHT platform. (**B**) 3D illustration of hydrodynamic trapping via streaming vortices. The (red) vibrating upright PZT plate is submerged in FC-40 oil. Together with the gray plates surrounding it, it forms a stable hydrodynamic trapping unit that can attract floating objects from all directions. (**C**) Top view image of the upright PZT array. Blue circles show the trapping points generated by each single unit. Ground pads on the PCB base are removed for clarity. Scale bar, 3 mm. (**D**) Illustration of droplet control. A droplet is moved in the xy plane in a programmed route by actuating specific units sequentially in a time (C). (**E** to **H**) Serial movement of a droplet with manual step control. The object is floating on the appropriate operating surface ($z = H$). Experiments include moving (E) water droplets, (F) silicon oil droplets, (G) aggregates of polystyrene particles (sized at 1 mm in diameter), and (H) 1× PBS buffer containing a single zebrafish embryo. Scale bar, 7 mm. Photo credits: Haodong Zhu, Duke University.

a quarter of the volume of a single upright PZT unit, on a scale of 6 mm by 6 mm on the xy plane (Fig. 2, A and B). Using a simple Gaussian distribution for the vibration amplitude on the xz plane and actuating only one of the four half-PZT plates, a 3D flow field was numerically simulated (Fig. 2C, note S2, and fig. S3). The flow field can be divided into two parts based on different z positions. The flow below the top of the PZT plate (i.e., the "edge plane" at $z = 5$ mm) still preserves the initial pattern with outflow in the y direction, while between the edge plane and the top layer at the fluid-air interface (i.e., the "operating surface" at $z = H$), a transition in the y direction combines with the backflow in the x direction to generate a stable trapping point in the operating surface. When we calculate the corresponding vorticity field, $\boldsymbol{\omega} = \nabla \times \mathbf{u}$, we can see a stable vortex tube (i.e., a high-vorticity region with constant radius in the 3D area) being generated from the bottom to the edge plane and then bending to propagate in the $+x$ direction (Fig. 2D). The shape of the vortex tube in Fig. 2D indicates that there is a pair of horseshoe vortices on both sides of the PZT, as shown in Figs. 1B
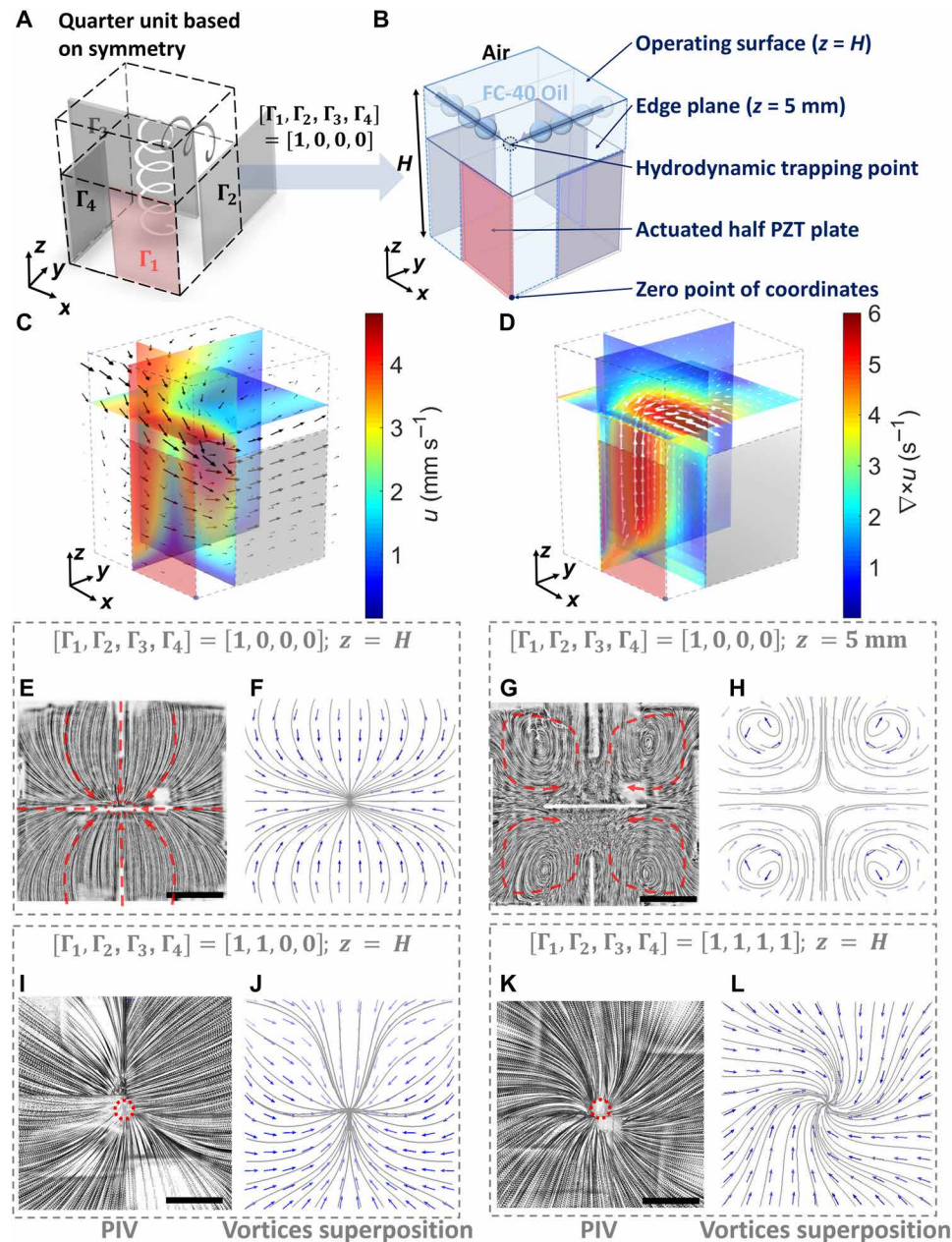
Fig. 2. The attraction mechanism behind a single AHT unit. (**A** and **B**) Because of symmetry, only a quarter unit needs to be modeled. (**C**) 3D numerical simulation result of the velocity field in a quarter unit. The color map shows the amplitude, and black arrows show the direction. (**D**) 3D simulation result of the vorticity field in a quarter unit. The white arrows represent the direction of the vorticity, and the color map indicates the intensity of the vortex. Three orthogonal planes are selected to show the shape of the vortex. (**E** to **H**) Flow field at the x plane operating surface (E and F) and edge y plane (G and H) obtained from microparticle tracking (E and G) and numerical simulations of the vorticity (F and H), respectively. Both (E) and (F) show the hydrodynamic trap in the center. For modeling results, the solid lines represent streamlines, and the colored arrows point in the direction of velocity at that point. (**I** to **L**) Combined flow field at the xy plane operating surface when two (I and J) and four (K and L) adjacent units are actuated. Both results from particle image velocimetry (I and K) and the simplified vortex-based model (J and L) show a new trap forming at the original trapping points (red circle). PIV, particle image velocimetry. Scale bars, 3 mm.

and 2A. Both vortex tubes share the same shape but propagate in opposite directions. They both originate near the bottom, propagate up in the z direction, and bend to cross over the height of the barrier in the x direction. This streaming shape agrees well with other previous works using a vibrating cantilever in a fluid (*33*, *34*), but with different applied frequencies. The high-vorticity area does not extend to the operating surface nor to the hydrodynamic trap-

ping point, as shown in Fig. 2B, indicating that this omnidirectional attraction can be considered a far-field effect of both vortex tubes generated by shaping the acoustic streaming.

Prediction and control of the flow field on the operating surface

After obtaining the shape of the vortex pairs, a simplified theoretical model can be used to describe the flow field and to explain the

trapping effect (note S3). On the basis of the numerical simulation results, the vortex tube is time independent, and the Reynolds number (Re) of the system, with a speed u^*, estimated from the average speed of droplet movement, and characteristic length scale D^* of the geometric scale of the structure (i.e., half the width of the upright PZT), is much smaller than the critical value for turbulence transition over a flat plate (35). This low Re satisfies the quasi-steady and laminar flow conditions. Thus, we can simplify the horseshoe vortex tube into three straight segments and use the Biot-Savart law to estimate the induced speed by a single section of the vortex tube with a circulation Γ_i and the spatial positions of its starting and ending points. For the simulation, we can simplify Γ_i as equal within each vortex segment and is only related to input power. Within the simplest actuation mode, all units have only either 0/1 states and share the same input voltage, V_{in}, so the generated vortices have the same magnitude Γ_i for all the sections. As only one of the four PZT units on the side of the symmetric model of the quarter unit is actuated, we can number the PZTs and represent this single-unit actuation using a combination of the on/off status of the surrounding units, namely, $[\Gamma_1, \Gamma_2, \Gamma_3, \Gamma_4] = [1,0,0,0]$ (Fig. 2A).

By combining the contribution of the six different parts (i.e., three segments on each side) of the vortex tubes and their mirror images along the operating surface to balance the z direction speed, we can get an approximation of the flow field $\mathbf{u}(\mathbf{\chi})$ generated at any spatial point $\mathbf{\chi}$ near the hydrodynamic trap. We use two xy cross sections to help validate this vortex-based simplified model. The resulting flow field on the operating surface agrees well with both the experimental and numerical simulation results (Fig. 2, E and F, and fig. S3B). However, because we ignore the existence of plate barriers that are submerged in the liquid, the predicted flow field on the edge plane only preserves part of the shape characteristics when comparing the experimental and simulation results. We can still observe four vortices, and we observe that they are not deformed (Fig. 2, G and H, and fig. S3C).

To perform more complicated manipulation processes, multi-unit actuation is needed. On the basis of experimental observations, if multiple adjacent units are actuated, a new hydrodynamic trap will be formed between the previous stable points. As shown in previous works, when pressure is assumed as small amplitude deviations, the pressure field from different actuated units that drives the acoustic streaming can be linearly superimposed (36, 37). Although opposing units generate some interactions with the pressure field, this overlapping effect is small compared with the total pressure field generated as the pressure has a maximum amplitude in the top middle part of the PZT. Because of the overall linearity of the system, this effect can be extended to the solution of the total governing equation (36) and also the total flow field. Using this theoretical model, we show that the total flow field generated by multiunit actuation can be simply expressed as a linear combination of flow fields resulting from single-unit actuation, with only minor modifications in the pressure amplitude (note S4). The linear characteristics of the model make it possible to manipulate and predict the combined flow field when multiple PZT units are actuated. Some basic situations including actuation of two ($[\Gamma_1, \Gamma_2, \Gamma_3, \Gamma_4] = [1,1,0,0]$; Fig. 2, I and J) and four ($[\Gamma_1, \Gamma_2, \Gamma_3, \Gamma_4] = [1,1,1,1]$; Fig. 2, K and L) adjacent units are shown, respectively, and the numerically generated flow field at the operating surface agrees well with the experimental results.

Modification of the flow field using different barrier arrays

To examine how this flow pattern changes based on any surrounding structures, we also inserted other barriers (made by PZT plates or plastic plates of identical size) around the submerged, single, upright PZT unit and measured the related radial flow velocity at $z = H$ near the center of the PZT plate, as a reference (Fig. 3). The fluid height H is set at 8 mm, while the height of the upright PZT is fixed at 5 mm (which is submerged 3 mm below the liquid surface). The center-to-center distance between different PZT units/blocking structures is set at 6 mm, and the input voltage V_{in} varies from 5, 6.5, and 8 Vpp for each structure (note S5 and figs. S4 and S5). Maintaining the symmetry of the unit, five different barrier arrangements (Fig. 3, A to E) are tested to partially block and modify the flow field near the plate in the center. To quantify how the flow field is being modified, we measured the flow trajectory around a single PZT plate and the speed profile in polar coordinates for each condition (Fig. 3, F to T, note S6, and fig. S6), to see whether it makes a difference in attracting/repelling characteristics and to understand how the flow speed changes based on different electric inputs to the central plate.

Compared with bare plate actuation as shown previously (Fig. 3F, K, and P, and fig. S2), the additional parallel barriers do not have an apparent effect on the original flow field but only slightly increase the repelling flow. The focus point is still at the center of the plate, but more extended in the y direction than the original flow field and is still unstable for the same reason as the original basic flow field (Fig. 3G, L, and Q). The insertion of additional vertical barriers significantly constrains the flow field and changes the attracting direction (Fig. 3H, M, and R). When two pairs of vertical barriers are added, they changed the main axis of attraction and rotate the attracting direction axis by approximately 45°. When the input energy increases, the flow field on top transforms from an all-repelling to an all-attracting behavior (Fig. 3I, N, and S). Only when both vertical and parallel constraints are added does omnidirectional attraction begin to reappear with similar radial velocities but at different angles. Although the flow field is constrained to a very large extent when given a comparable high voltage input (i.e., at 8 Vpp) on a single upright PZT unit, an omnidirectional attraction region above the unit will be created (Fig. 3J, O, and T). With the repelling flow eliminated on the top layer of the fluid, the hydrodynamic trapping point is now stable. This stable and symmetric unit geometry makes it possible to scale up this platform.

Experimental characterization of motion control

When a single upright PZT unit is actuated, the flow field generated around the floating object will quickly start to drag the droplet. This is mainly based on the shear force between the boundary of the object and the carrier fluid. The droplet will gradually synchronize with the acoustic streaming and be stabilized in the hydrodynamic trap. Specifically, when the floating droplet is near a side of the active PZT, it will be automatically translated in the $\pm x$ directions toward the PZT following a hydrodynamic gradient. Eventually, the object is stabilized above one of the submerged, upright PZT units. Figure 4 (A and D) schematically shows this typical motion of a water droplet, which can be considered as one "time step," with a top view of droplet movement along the x axis and a schematic cross-sectional view of the xz plane illustrating the movement motion above the oil.
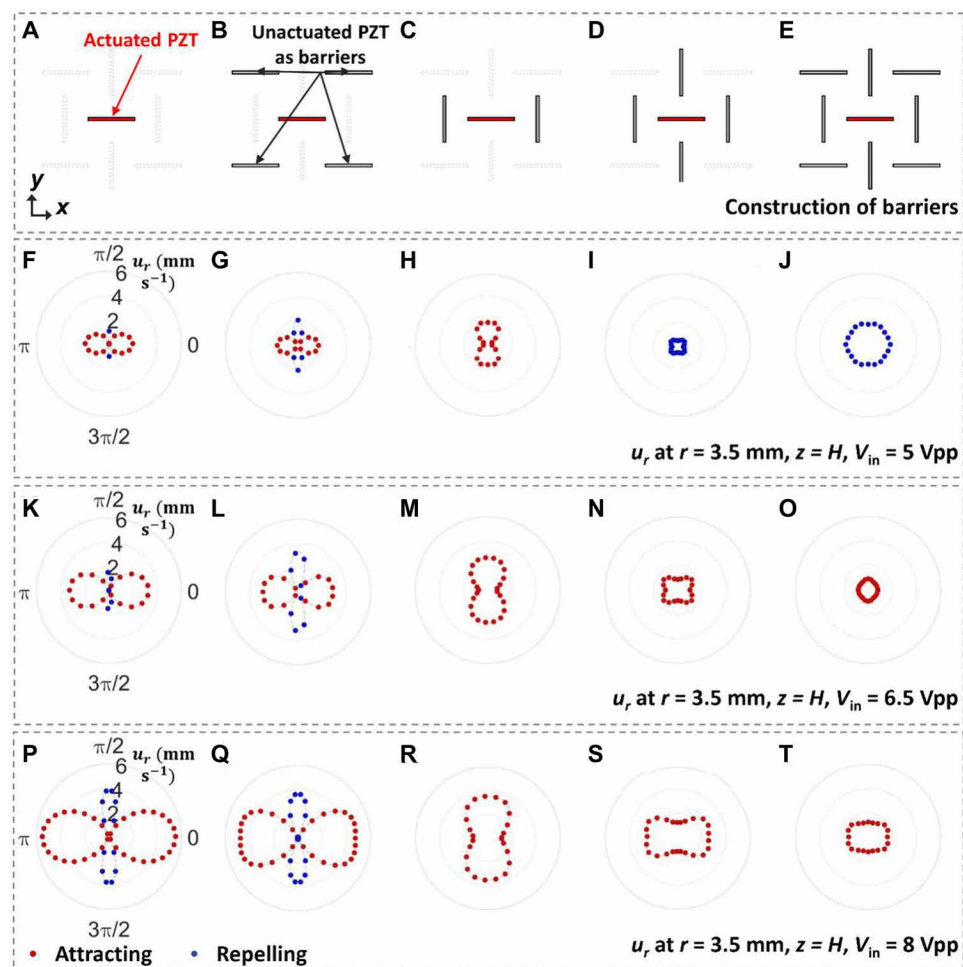
Fig. 3. Flow fields at the operating surface as generated by different barrier configurations of an AHT. (**A** to **E**) Diagrams of the top view of an actuated upright PZT plate and different configurations of barriers around it. Five different configurations are investigated: (A) a bare PZT plate without barriers, (B) four horizontal barriers, (C) two vertical barriers, (D) four vertical barriers, and (E) four vertical plus four horizontal barriers. For each figure, the PZT in the center is actuated. All other PZTs shown in gray serve as barriers. (**F** to **T**) The radial velocity field for different configurations, as captured at 3.5 mm around the center, at $z = H$. The figures can be divided into three groups, each of them covers all the aforementioned configurations (A to E) and uses different input voltage V_{in}: 5 (F to J), 6.5 (K to O), and 8 Vpp (P to T), respectively. Red dots represent attractive forces, while the blue dots represent repulsion at a specific angle. The scale of the positive/attractive speed is shown in each figure. For clarity, all negative/repelling speeds are doubled in the figure. Details of the approach to obtain the radial velocity from particle tracking results are in the Supplemental Materials note S6 and fig. S6.

Although the barrier arrangement is the main factor determining the stability of the hydrodynamic trap, the performance of the platform is also influenced by the fluid height H, input voltage V_{in}, and the size of the droplet or particle that is manipulated D. To determine how these parameters affect the droplet movement to optimize the system, it is necessary to further analyze the details of the trapping modes of this scaled-up platform. Thus, we keep V_{in} at 8 Vpp according to the result from Fig. 3T and perform a parametric scan with variable [D, H] groups. For all routing experiments, water droplets are chosen as the objects for tweezing as they maintain their shape and are easier to adjust their volume.

While the trapping is omnidirectional on the operating surface, under most working conditions, motion in two directions is necessary to move the droplet along any line connecting adjacent hydrodynamic traps toward a target destination (i.e., along the x or y axis). Because the movement between each PZT unit is reversible, we can move a droplet of a certain size between two units by actuating each

unit in an alternating manner (Fig. 4, E and F, and note S7). Because of the orthogonality of adjacent units, the process of "moving backward" in the x axis follows a different fluid path. Taking advantage of the symmetry of each unit, only two different modes are necessary to cover all the characteristics of moving in rectangular paths. We define them as the "longitudinal mode" (returning in a direction parallel to the actuated PZT, as seen in Fig. 4, A and B) and the "lateral mode" (returning in a vertical direction of the plane parallel with the operating surface and toward the actuated PZT; Fig. 4, C and D) for droplet movement. The 3D numerical simulations of the flow field (Fig. 2C) also show that these two modes are generated by different mechanisms. The longitudinal mode follows the original pattern of the backflow created directly by the main outflow of the upright PZT. However, the lateral mode is created by the bending of the main outflow on the surrounding barrier.

On the basis of parametric analysis (Fig. 4, G to J), we used a color map to plot the average speed of each step, $\bar{u}$, versus droplet diameter,
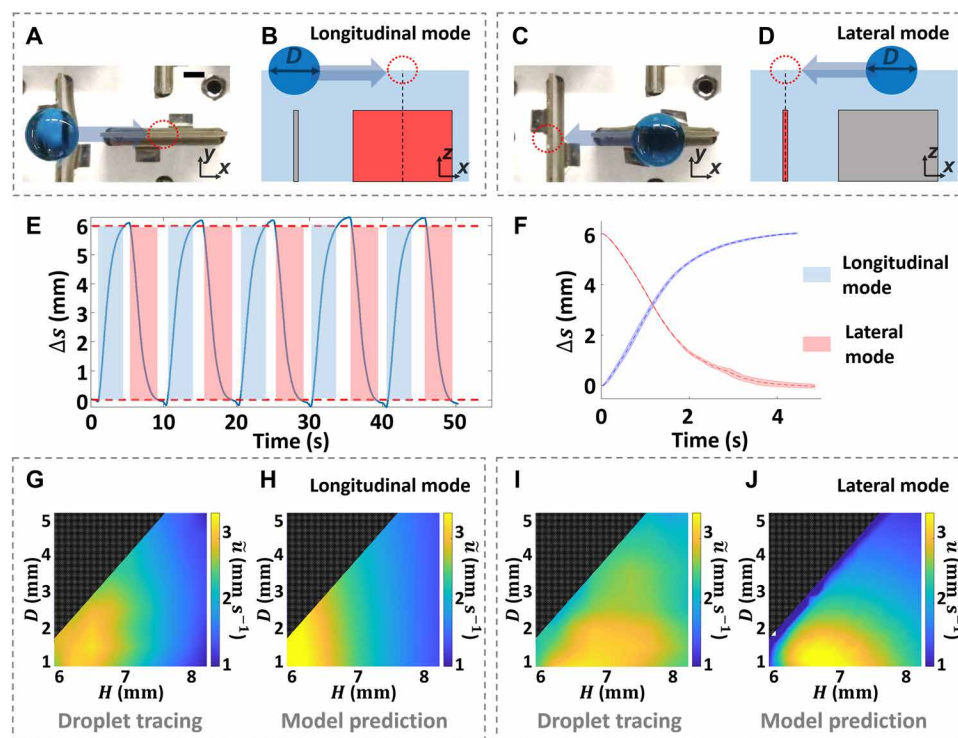
Fig. 4. Two-directional velocity profiles of the 4 × 4 AHT prototype. (**A** to **D**) Top view image of droplet movement along the *x* axis in (A) the longitudinal mode and in (C) the lateral mode, respectively, and a schematic cross-sectional view of the *xz* plane illustrating the movement beneath the oil (B and D), with the actuated unit in red. Scale bar, 1 mm. (**E**) Example of droplet tracing in both longitudinal and lateral modes. A droplet of diameter *D* is moved back and forth between two adjacent units with a step time set at 5 s. The movement between two thresholds (red dotted lines) is recorded to calculate the average speed $\bar{u}$. (**F**) Averaged trajectories of the longitudinal and lateral modes, with the shaded area showing the standard deviations. (**G** to **J**) Parametric analysis of $\bar{u}$ by varying *H* and *D* in both modes. The resulting tracing experiments (G and I) and droplet movement estimates using the vortex-based flow field model (H and J; note S8 and fig. S7). The black plaid areas indicate the nonfunctional parametric region where there is direct contact of the droplet to the PZT. Photo credits: Haodong Zhu, Duke University.

D, and the carrier fluid height, *H*, under both longitudinal and lateral modes. Experimental results (Fig. 4, G and I) agree well with the analysis based on the velocity field $\mathbf{u}(\chi)$ and fluid-droplet interaction (Fig. 4, H and J, note S8, and fig. S7), which show different parameter settings for the longitudinal and lateral modes, if high-speed operation is desired. The longitudinal mode has a large applicable range on droplet size *D* (i.e., 1 to 3 mm) compared with the lateral mode. Meanwhile, the lateral mode is more stable with *H*, where the high-speed (i.e., >3 mm/s) area of operation covers the *H* = (6.5 and 7.5 mm) region. However, almost all the parameters tested with this platform (except the ones that will cause direct contact of the droplet to the PZT) will have an average speed of more than 1.2 mm s^{-1}, which again demonstrates the robustness of this platform's operational parameters.

Digital droplet handling using single and multiple units

As mentioned previously, if the hydrodynamic traps are actuated in a programmed spatial and sequential manner, then a droplet floating on the carrier oil can be controlled and moved in a specific path (Fig. 1, C and D). After the performance of a single unit has been optimized, we then built a control system for routing single or multiple droplets. An Arduino-based program and microcontroller were used to schedule the route of the droplet (note S9 and fig. S8). Basically, the spatial route in the *xy* plane is first identified in terms of sequential trapping points, and then the spatial route is translated

into a step-based control scheme, in which each selected transducer is turned on or off sequentially based on the appropriate time step (Fig. 5A). For all routing experiments, V_{in} remains at 8 Vpp and the step time is set at 5 s based on the parametric scanning outcome of the average velocity.

For single-droplet routing, we first performed experiments using the upright PZT array to translate a 30-μl droplet along four different paths and trace out the letters "D," "U," "K," and "E" (movie S2). The floating droplet can be observed to be manipulated smoothly in a curved path. Figure 5B presents stacked, composite images acquired during the dynamic manipulation. The images show that the particle trajectories precisely traced out the four letters, and the curved parts in the letters "D" and "U" are achieved by actuating the diagonal unit. Because of the manner of the single-unit attraction, the back and forth curvature between two diagonal units is different, as shown in the trace of the letter "K."

To further validate the performance of the 16-unit prototype platform, we also perform a simple chemical detection assay as validation of the ability to perform a reaction cascade. Gold nanoparticle (AuNP)–based color detection has long been used as a quick method for measuring the concentration of a target biochemical compound. Many color detection mechanisms are based on the aggregation of AuNPs, as the absorption spectrum will change in the visible light region based on the size of AuNP aggregates. This mechanism is effective, especially when the AuNPs carry a different
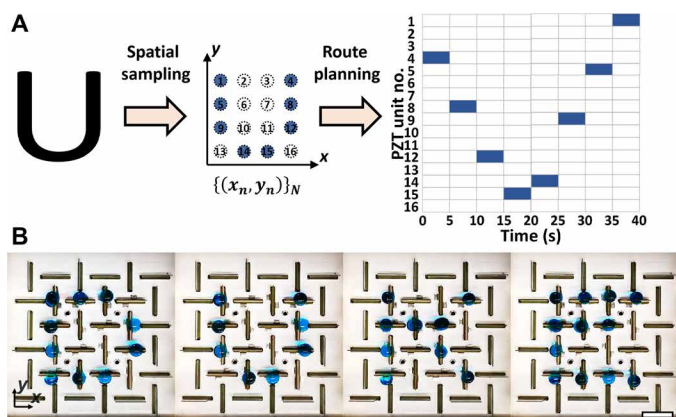
Fig. 5. Programmable routing of a single droplet via AHT. (A) Demonstration of the control scheme for moving a single droplet. The desired path is first sampled to a line of scattered spatial points in the *xy* plane, then is mapped to a vector containing the corresponding sequence of PZT unit numbers, and then mapped to a step-based control scheme. (**B**) Automatic routing of a single droplet is shown in a stacked composite image of droplets. We choose four routes, with the time-elapsed images corresponding to the letters "D," "U," "K," and "E." The full process can be viewed in movie S2. The floating droplet is moved along the programmed route in either straight or curved lines. All step times are set to be 5 s, and all the route shapes are time stacked once per step. The color of the droplet is digitally modified to get darker as the route progresses, for clarity. Scale bar, 7 mm. Photo credits: Haodong Zhu, Duke University.

charge with respect to the target compound. Positive-charged AuNPs are used often to detect chain-structured chemicals with a negative charge, such as DNA.

In this demonstration experiment, we choose cysteamine-modified AuNP as the label indicator and heparin as the detection target according to previous works (*38*, *39*). Heparin, also known as unfractionated heparin, is a medication and a naturally occurring glycosaminoglycan. It is used as an anticoagulant reagent (i.e., anticoagulant I) and also in the treatment of heart attacks and unstable angina (*40*). The chemical reaction mechanism is shown in Fig. 6A. For each step of the chemical reaction assay on the platform, a 25-μl AuNP droplet with a concentration of 7.1×10^{-3} M is first combined with a 10-μl droplet containing the heparin target with concentrations varying from 100 to 0.001 μg/ml. After sufficient mixing, a 10-μl Britton-Robinson (B-R) buffer droplet is added for pH adjustment. By repeating this reaction route, we achieve effective detection of heparin with a concentration range from 0.1 to 100 μg/ml (Fig. 6B), which is comparable to the accuracy of other previous work on heparin detection (*38*, *39*).

The control scheme for this detection assay is similar to that in Fig. 5A, but with the actuation of multiple units to realize several different functions (Fig. 6B). The images show different steps of the assay including droplet merging, mixing, and incubation on the platform, as shown in Fig. 6 (C to F). The three droplets were previously attracted over three different corner units of the platform and then combined using a routing program. The first mixing step is faster and requires only several movement steps. The second step involves combining the mixed droplet with the B-R buffer droplet. The whole reaction system is in the center of the platform for 15 min of mixing and incubation under room temperature. During the incubation process, we actuate four units near the center to create a vortex inside the droplet as predicted by the theoretical model

(Fig. 2, K and L). After sufficient reaction time, we extract the whole droplet via a pipette and measure its absorption spectrum using a microplate reader. For most target concentrations, the color starts to change after 5 min and stabilizes after 10 min. Spectrum results show the main absorption peaks at 523 nm for the monodispersed AuNP and a peak near 650 nm, which is shifting right as the target concentration decreases. This result indicates the aggregation of AuNPs. These results fit with theoretical expectations as the size of the aggregates changes gradually based on the target concentration. The AHT platform thus enables simplified, automated, and parallel detection, which can track the progression of the reaction during an assay.

DISCUSSION

In this work, we report a new AHT platform based on modulated acoustic streaming. We have analyzed the trapping mechanism and realized accurate manipulation of particles and liquid droplets based on the flow field produced by stable pairs of vortices. Compared with previous tweezer technologies, AHT brings three main advantages: dynamic control and accurate prediction of the flow field on the operating surface, convenience in device fabrication and system setup, and reliable uniformity in performance with low power input. On the basis of a submerged array of upright plates, a stable flowing pattern is generated via modified acoustic streaming. This result enables control of a nonlinear mechanism for hydrodynamic trapping. While previous acoustic streaming tweezers have realized dynamic control of floating objects by controlling the on/off state of local streaming patterns, in our AHT mechanism, the location of the hydrodynamic trap can be predicted and modulated at any point in the operating surface by actuating single or multiple upright PZT units at the same time. This improvement of the AHT mechanism allows for precision control of the fluid field for complex manipulation processes. The reciprocal array pattern and digitized electronic control system allow each upright PZT unit to manipulate droplets with a wide range of volumes (a few nanoliters to hundreds of microliters) using a low power input (8 Vpp per unit). During characterization tests, this robust platform works stably over a wide range of operating parameters.

From the results of droplet path tracing experiments, this AHT platform works with a low variance between each route (<2% coefficient of time variation). Considering the design of the prototype, the variance is most possibly caused by two reasons: (i) the slight variance in the electrical properties between each PZT plate and (ii) manually inserting each upright PZT unit to the polychlorinated biphenyl (PCB) during fabrication. The variance can further be reduced with improvements in precision milling of PZT plates and automated pick-and-place positioning of components on the PCB. As the feasibility of the vortex-based model only depends on the *Re* but not the scale of each unit, and the variance during fabrication is fixed in scale, we can further scale down the unit size while maintaining a reasonable variance by applying improved fabrication techniques. Thus, the platform can potentially manipulate smaller objects (such as a single cell) based on a similar tweezing mechanism. In addition, the control algorithm can be improved with a digital feedback loop. This will improve the spatial accuracy of the hydrodynamic trap by dynamically tuning V_{in} continuously to each unit. As mentioned in note S4, new trapping points can be generated by using a different combination of actuation power to the individual units. Hence, continuous control should allow for the generation of
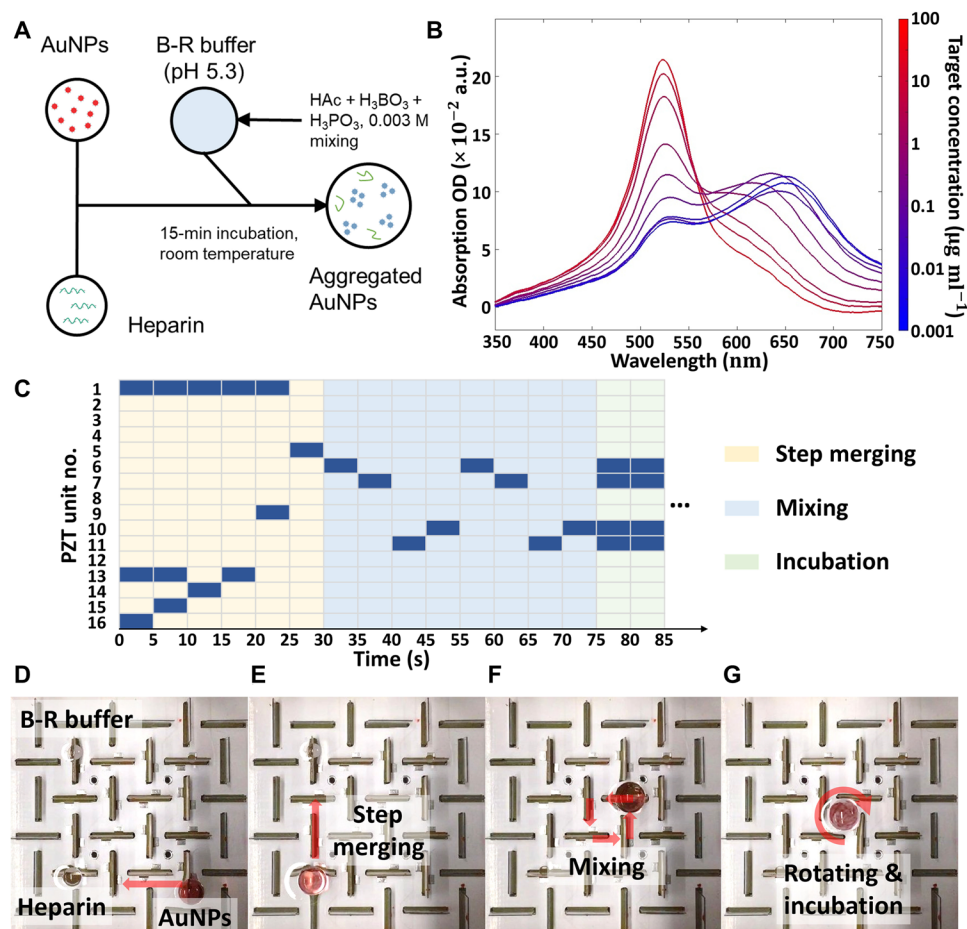
Fig. 6. Demonstration of a cascade reaction on the AHT platform. (**A**) Reaction mechanism for AuNP-based heparin detection. (**B**) The absorption spectrum for the detected heparin at different positions. We can observe a peak representing scattered AuNPs gradually decrease and another peak indicating the aggregated AuNPs gradually increase and shift to the right side. a.u., arbitrary units. (**C**) Flow control scheme used in this detection procedure. Red blocks represent the step-based actuation events, and different background colors represent the three different operational phases: merging, mixing, and incubation. (**D** to **G**) The reaction cascade as performed on the AHT platform. During the assay, three droplets are trapped on three different PZT units. The AuNP droplet first combines with the heparin droplet, then with the B-R buffer droplet. This combined droplet is then moved to the center for mixing and incubation. The full process is recorded in movie S2. Photo credits: Haodong Zhu, Duke University.

trapping points at any point on the operating surface and result in even more complex droplet paths.

In summary, AHT provides a hydrodynamic-based approach for a contactless, biocompatible, and low-power tweezer. This new trapping mechanism has been theoretically modeled and experimentally verified. The geometric and operational parameters have been optimized. This platform has achieved more sophisticated dynamic control of droplet paths at low power levels (i.e., <8 Vpp and 11 MHz per unit). We believe that this AHT platform will advance a wide range of applications, requiring multistep reaction assays such as drug or infection screening.

MATERIALS AND METHODS
Device fabrication
The PCB plates (JLCPCB Inc., Shenzhen, China) is designed to be 1.2 mm thick with two layers and patterned slots sized at 7.2 mm by 1 mm. The joint structure is 3D printed using a multijet at a spatial resolution of 0.1 mm (Bluesmith, Duke University, NC, USA). PZT

plates used for single units are 7 mm by 7 mm by 0.2-mm-thick piezo ceramic plates (SMPL7W7T02412, STEM Inc., FL, USA).

For most of the manipulation experiments discussed in the paper, we use the design shown in Fig. 2A with distance between unit centers, ΔL, of 6 mm and height of the oil layer, H, as 8 mm. The choice of these system parameters is based on the simulation results of the vortex tube generated (figs. S4 and S5). More information of the influence of different system parameters is discussed in note S5.

Experimental setup
The carrier oil is the 3M Fluorinert FC-40 (Parallax Technology Inc., MA, USA). This forms the operating surface. To increase the viscosity of the carrier oil and enhance the spatial stability of the floating droplets, we dissolve 0.5% Teflon (AF1600, Dupont Co., DE, USA) into the FC-40 oil. The AHT device is powered by a function generator (DG 3012C, Teletronics Technology Corporation, PA, USA) and an amplifier (25A250A, Amplifier Research, USA) with an 11-MHz sinusoidal AC signal in all experiments. A relay array (Ningbo Songle Relay Co., Ltd., China) and a microcontroller

(ELEGOO MEGA 2560, Elegoo Inc., USA) are used to control the power input to individual transducers. Both pad-based manual control and programmed control for the 16-unit prototype is written using the Arduino integrated development environment.

Flow field simulation

We used COMSOL Multiphysics for the flow field finite element method simulation. More details about the simulation parameters can be found in note S2, fig. S3, and table S1.

Flow field estimation using microparticles

For flow imaging, 30-μm-diameter silver particles (PMPMP-AG-1.9, Cospheric LLC, USA) are suspended in 3M Fluorinert FC-40 oil, and each single-unit actuation voltage is maintained at 8 Vpp. The resulting path lines are recorded by an Olympus upright microscope at 25 frames/s (fps). At steady-state conditions, the streamlines generated by acoustic streaming are identical to the calculated values. For flow field results, time-elapsed stacks of images from different parts are combined to generate the final composite image. We analyzed the speed of particles using a C++ program (Microsoft Corp., USA) and calculated the radial velocity speed profile using a MATLAB program. The method for the flow field and radial velocity profile measurements is detailed in note S6 and fig. S6.

Reagents and materials for the heparin detection experiment

Following a previously published protocol for heparin detection (38), we use 30-nm-diameter AuNP (#J6917, 2.5% Wt., Nanopartz Inc., USA/Canada). The heparin sample (heparin sodium salt from porcine intestinal mucosa, ≥180 United States Pharmacopeia units/mg) and all other reagents used in the cascade reaction process are from Sigma-Aldrich (Darmstadt, Germany).

SUPPLEMENTARY MATERIALS
Supplementary material for this article is available at http://advances.sciencemag.org/cgi/content/full/7/2/eabc7885/DC1

REFERENCES AND NOTES

1. M. L. Juan, M. Righini, R. Quidant, Plasmon nano-optical tweezers. *Nat. Photonics* **5**, 349–356 (2011).
2. K. Choi, A. H. C. Ng, R. Fobel, A. R. Wheeler, Digital microfluidics. *Annu. Rev. Anal. Chem.* **5**, 413–440 (2012).
3. S. K. Cho, H. Moon, C.-J. Kim, Creating, transporting, cutting, and merging liquid droplets by electrowetting-based actuation for digital microfluidic circuits. *J. Microelectromech. Syst.* **12**, 70–80 (2003).
4. J. Lee, H. Moon, J. Fowler, T. Schoellhammer, C.-J. Kim, Electrowetting and electrowetting-on-dielectric for microscale liquid handling. *Sensors Actuators A Phys.* **95**, 259–268 (2002).
5. M. G. Pollack, R. B. Fair, A. D. Shenderov, Electrowetting-based actuation of liquid droplets for microfluidic applications. *Appl. Phys. Lett.* **77**, 1725–1726 (2000).
6. P. K. Wong, T.-H. Wang, J. H. Deval, C.-M. Ho, Electrokinetics in micro devices for biotechnology applications. *IEEE/ASME Trans. Mechatron.* **9**, 366–376 (2004).
7. N. Francois, H. Xia, H. Punzmann, P. W. Fontana, M. Shats, Wave-based liquid-interface metamaterials. *Nat. Commun.* **8**, 14325 (2017).
8. K. Latifi, H. Wijaya, Q. Zhou, Motion of Heavy Particles on a Submerged Chladni Plate. *Phys. Rev. Lett.* **122**, 184301 (2019).
9. A. Ozcelik, J. Rufo, F. Guo, Y. Gu, P. Li, J. Lata, T. J. Huang, Acoustic tweezers for the life sciences. *Nat. Methods* **15**, 1021–1028 (2018).
10. G. Destgeer, H. J. Sung, Recent advances in microfluidic actuation and micro-object manipulation via surface acoustic waves. *Lab Chip* **15**, 2722–2738 (2015).
11. M. Wu, A. Ozcelik, J. Rufo, Z. Wang, R. Fang, T. J. Huang, Acoustofluidic separation of cells and particles. *Microsyst. Nanoeng.* **5**, 32 (2019).
12. F. Petersson, L. Åberg, A.-M. Swärd-Nilsson, T. Laurell, Free flow acoustophoresis: Microfluidic-based mode of particle and cell separation. *Anal. Chem.* **79**, 5117–5123 (2007).
13. T. Franke, A. R. Abate, D. A. Weitz, A. Wixforth, Surface acoustic wave (SAW) directed droplet flow in microfluidics for PDMS devices. *Lab Chip* **9**, 2625–2627 (2009).
14. L. Y. Yeo, J. R. Friend, Ultrafast microfluidics using surface acoustic waves. *Biomicrofluidics* **3**, 12002 (2009).
15. F. Guo, Z. Mao, Y. Chen, Z. Xie, J. P. Lata, P. Li, L. Ren, J. Liu, J. Yang, M. Dao, S. Suresh, T. J. Huang, Three-dimensional manipulation of single cells using surface acoustic waves. *Proc. Natl. Acad. Sci.* **113**, 1522–1527 (2016).
16. M. Gedge, M. Hill, Acoustofluidics 17: Theory and applications of surface acoustic wave devices for particle manipulation. *Lab Chip* **12**, 2998–3007 (2012).
17. D. J. Collins, B. Morahan, J. Garcia-Bustos, C. Doerig, M. Plebanski, A. Neild, Two-dimensional single-cell patterning with one cell per well driven by surface acoustic waves. *Nat. Commun.* **6**, 8686 (2015).
18. J. Reboud, Y. Bourquin, R. Wilson, G. S. Pall, M. Jiwaji, A. R. Pitt, A. Graham, A. P. Waters, J. M. Cooper, Shaping acoustic fields as a toolset for microfluidic manipulations in diagnostic technologies. *Proc. Natl. Acad. Sci.* **109**, 15162–15167 (2012).
19. A. Marzo, M. Caleap, B. W. Drinkwater, Acoustic virtual vortices with tunable orbital angular momentum for trapping of mie particles. *Phys. Rev. Lett.* **120**, 044301 (2018).
20. L. Cox, K. Melde, A. Croxford, P. Fischer, B. W. Drinkwater, Acoustic Hologram Enhanced Phased Arrays for Ultrasonic Particle Manipulation. *Phys. Rev. Appl.* **12**, 064055 (2019).
21. Y. Li, X. Jiang, B. Liang, J. Cheng, L. Zhang, Metascreen-based acoustic passive phased array. *Phys. Rev. Appl.* **4**, 024003 (2015).
22. Z. Tian, S. Yang, P.-H. Huang, Z. Wang, P. Zhang, Y. Gu, H. Bachman, C. Chen, M. Wu, Y. Xie, T. J. Huang, Wave number–spiral acoustic tweezers for dynamic and reconfigurable manipulation of particles and cells. *Sci. Adv.* **5**, eaau6062 (2019).
23. Z. Tian, C. Shen, J. Li, E. Reit, H. Bachman, J. E. S. Socolar, S. A. Cummer, T. J. Huang, Dispersion tuning and route reconfiguration of acoustic waves in valley topological phononic crystals. *Nat. Commun.* **11**, 762 (2020).
24. M. Wiklund, R. Green, M. Ohlin, Acoustofluidics 14: Applications of acoustic streaming in microfluidic devices. *Lab Chip* **12**, 2438–2451 (2012).
25. J. S. Bach, H. Bruus, Bulk-driven acoustic streaming at resonance in closed microcavities. *Phys. Rev. E* **100**, 023104 (2019).
26. N. Nama, P.-H. Huang, T. J. Huang, F. Costanzo, Investigation of acoustic streaming patterns around oscillating sharp edges. *Lab Chip* **14**, 2824–2836 (2014).
27. D. J. Collins, Z. Ma, Y. Ai, Highly localized acoustic streaming and size-selective submicrometer particle concentration using high frequency microscale focused acoustic fields. *Anal. Chem.* **88**, 5513–5522 (2016).
28. D. J. Collins, Z. Ma, J. Han, Y. Ai, Continuous micro-vortex-based nanoparticle manipulation via focused surface acoustic waves. *Lab Chip* **17**, 91–103 (2017).
29. D. Ahmed, A. Ozcelik, N. Bojanala, N. Nama, A. Upadhyay, Y. Chen, W. Hanna-Rose, T. J. Huang, Rotational manipulation of single cells and organisms using acoustic waves. *Nat. Commun.* **7**, 11085 (2016).
30. Z. Mao, P. Li, M. Wu, H. Bachman, N. Mesyngier, X. Guo, S. Liu, F. Costanzo, T. J. Huang, Enriching nanoparticles via acoustofluidics. *ACS Nano* **11**, 603–612 (2017).
31. S. P. Zhang, J. Lata, C. Chen, J. Mai, F. Guo, Z. Tian, L. Ren, Z. Mao, P.-H. Huang, P. Li, S. Yang, T. J. Huang, Digital acoustofluidics enables contactless and programmable liquid handling. *Nat. Commun.* **9**, 2928 (2018).
32. P. Zhang, C. Chen, X. Su, J. Mai, Y. Gu, Z. Tian, H. Zhu, Z. Zhong, H. Fu, S. Yang, K. Chakrabarty, T. J. Huang, Acoustic streaming vortices enable contactless, digital control of droplets. *Sci. Adv.* **6**, eaba0606 (2020).
33. A. L. Facci, M. Porfiri, Analysis of three-dimensional effects in oscillating cantilevers immersed in viscous fluids. *J. Fluids Struct.* **38**, 205–222 (2013).
34. A. N. Nuriev, A. M. Kamalutdinov, A. G. Egorov, A numerical investigation of fluid flows induced by the oscillations of thin plates and evaluation of the associated hydrodynamic forces. *J. Fluid Mech.* **874**, 1057–1095 (2019).
35. K. Avila, D. Moxey, A. de Lozar, M. Avila, D. Barkley, B. Hof, The onset of turbulence in pipe flow. *Science* **333**, 192–196 (2011).
36. Q. Tang, J. Hu, S. Qian, X. Zhang, Eckart acoustic streaming in a heptagonal chamber by multiple acoustic transducers. *Microfluid. Nanofluid.* **21**, 28 (2017).
37. T. Freegarde, *Introduction to the Physics of Waves* (Cambridge Univ. Press, 2012).
38. R. Cao, B. Li, A simple and sensitive method for visual detection of heparin using positively-charged gold nanoparticles as colorimetric probes. *Chem. Commun.* **47**, 2865–2867 (2011).
39. X. Fu, L. Chen, J. Li, Ultrasensitive colorimetric detection of heparin based on self-assembly of gold nanoparticles on graphene oxide. *Analyst* **137**, 3653–3658 (2012).
40. K. D. McClatchey, *Clinical Laboratory Medicine* (Lippincott Williams & Wilkins, 2002).
41. L. E. Kinsler, A. R. Frey, A. B. Coppens, J. V Sanders, Fundamentals of acoustics, in *Fundam. Acoust. 4th Ed. by Lawrence E. Kinsler, Austin R. Frey, Alan B. Coppens, James V. Sanders, pp. 560. ISBN 0–471–84789-5. Wiley-VCH, December 1999.*, 560 (1999).
42. P. Hahn, I. Leibacher, T. Baasch, J. Dual, Numerical simulation of acoustofluidic manipulation by radiation forces and acoustic streaming for complex particles. *Lab Chip* **15**, 4302–4313 (2015).

43. J. Lei, P. Glynne-Jones, M. Hill, Acoustic streaming in the transducer plane in ultrasonic particle manipulation devices. *Lab Chip* **13**, 2133–2143 (2013).

44. G. G. Stokes, On the theories of the internal friction of fluids in motion, and of the equilibrium and motion of elastic solids. *Trans. Cambridge Philos. Soc.* **8**, (1880).

45. Q. Tang, J. Hu, Diversity of acoustic streaming in a rectangular acoustofluidic field. *Ultrasonics* **58**, 27–34 (2015).

46. Q. Tang, J. Hu, Analyses of acoustic streaming field in the probe-liquid-substrate system for nanotrapping. *Microfluid. Nanofluid.* **19**, 1395–1408 (2015).

47. J. Lighthill, Acoustic streaming. *J. Sound Vib.* **61**, 391–418 (1978).

48. C. Devendran, I. Gralinski, A. Neild, Separation of particles using acoustic streaming and radiation forces in an open microfluidic channel. *Microfluid. Nanofluid.* **17**, 879–890 (2014).

49. D. W. Moore, P. G. Saffman, The motion of a vortex filament with axial flow. *Philos. Trans. R. Soc. A* **272**, 403–429 (1972).

Citation: H. Zhu, P. Zhang, Z. Zhong, J. Xia, J. Rich, J. Mai, X. Su, Z. Tian, H. Bachman, J. Rufo, Y. Gu, P. Kang, K. Chakrabarty, T. P. Witelski, T. J. Huang, Acoustohydrodynamic tweezers via spatial arrangement of streaming vortices. *Sci. Adv.* **7**, eabc7885 (2021).

Science Advances

Acoustohydrodynamic tweezers via spatial arrangement of streaming vortices

Haodong Zhu, Peiran Zhang, Zhanwei Zhong, Jianping Xia, Joseph Rich, John Mai, Xingyu Su, Zhenhua Tian, Hunter Bachman, Joseph Rufo, Yuyang Gu, Putong Kang, Krishnendu Chakrabarty, Thomas P. Witelski and Tony Jun Huang

ARTICLE TOOLS	http://advances.sciencemag.org/content/7/2/eabc7885
SUPPLEMENTARY MATERIALS	http://advances.sciencemag.org/content/suppl/2021/01/04/7.2.eabc7885.DC1
REFERENCES	This article cites 45 articles, 5 of which you can access for free http://advances.sciencemag.org/content/7/2/eabc7885#BIBL
PERMISSIONS	http://www.sciencemag.org/help/reprints-and-permissions

Use of this article is subject to the Terms of Service